How heterogeneous microstructure determines mechanical behavior of laser powder bed fusion AlSi10Mg

Lubin Song[a], Lv Zhao[a,d,*], Lipeng Ding[b], Yaxin Zhu[a,d], Shuang Liang[a,d], Minsheng Huang[a,d], Aude Simar[c], Zhenhuan Li[a,d]

[a] *Department of Mechanics, School of Aerospace Engineering, Huazhong University of science and Technology, Wuhan, China*

[b] *Key Laboratory for Light-weight Materials, Nanjing Tech University, Nanjing, China*

[c] *Institute of Mechanics, Materials and Civil Engineering, UCLouvain, Louvain-la-Neuve, Belgium*

[d] *Hubei Key Laboratory of Engineering Structure Analysis and Safety Assessment, 1037 Luoyu Road, Wuhan, China*

Abstract

Laser powder bed fusion AlSi10Mg exhibits hierarchical and heterogeneous microstructure, which leads to anisotropic mechanical properties. The present work systematically investigated strength, ductility and their correlations to heterogeneous microstructure along different loading directions. Two AlSi10Mg samples presenting distinct features of Al-Si cellular structures and melt pool borders were analyzed, using combined tensile tests and digital image correlation measurements at both macro and micro scales. In addition, crystal plasticity modeling and simulation were conducted to reveal the deformation behavior and propensity to damage in the melt pool interiors and at the melt pool borders. Strain localizations are found in both the building direction and the perpendicular direction, due to weaker melt pool border and soft grain orientation, respectively. With the experimental and numerical results, it is

* Corresponding author: lvzhao@hust.edu.cn (L. Zhao).

demonstrated that the strength anisotropy mainly originates from the elongated Al-Si cellular structure, while the melt pool border plays a secondary role. Moreover, the ductility and its anisotropy appear to be determined by combined effects of strain localization, propensity to damage and constraints to crack formation. The findings of the present work unveil clearly how hierarchical and heterogeneous microstructure renders the macroscopic mechanical properties of additively manufactured Al alloys in different loading directions.

Keywords

Laser powder bed fusion; Microstructure; HR-DIC; Strain localization; Crystal plasticity

1. Introduction

Laser powder bed fusion (LPBF) is one of the most popular metal additive manufacturing techniques [1-3]. It enables manufacturing of highly complex geometries via layer-by-layer building strategy and hence presents a promising applicability in aerospace, automotive and biomedical industries [4-8]. Among the various LPBF metals, aluminum alloys, especially the Al-Si system, stand out for their excellent printability, good corrosion resistance and high strength to density ratio [9-11]. LPBF AlSi10Mg is an epitome for the development and application of additive manufacturing technology [12-14].

The intrinsic characteristics of the LPBF process, i.e. excessively high cooling speed, strong temperature gradient and layer-by-layer building scheme lead to hierarchical and heterogeneous structures [15-17]. The microstructure of LPBF AlSi10Mg spans over several scales: nanoscale solute atom clusters [18] and precipitates [19], microscale Al-Si cellular structures [20] and mesoscale melt pools (MP) [21]. The Al-Si cellular structure is composed of elongated Al cells enclosed by interconnected Si-rich eutectic phase [22-24]. The melt pool is constituted by an aggregate of Al-Si cells presenting different geometrical features and crystallographic orientations [24, 25]. According to the size and connectivity of the Si-rich networks, a MP can be divided into three regions, namely the fine melt pool (FMP), the coarse melt pool (CMP) and the heat affected zone (HAZ), the latter two constituting the melt pool border (MPB) [26-29]. In addition, the particular thermal field of the LPBF process renders AlSi10Mg columnar grains in MP interiors exhibiting a weak <001> fiber texture and equiaxial grains at MPBs presenting random orientations [30].

The abovementioned microstructure imparts a higher strength to LPBF AlSi10Mg compared with the as-cast counterparts [25, 31, 32]. However, it also leads to anisotropy in mechanical properties that remains an important hurdle yet to be overcome [24]. Indeed, LPBF AlSi10Mg generally presents lower strengths and elongation to failure when loaded along the building direction (i.e. vertical direction), while it shows a stronger strain hardening capacity when loaded along the perpendicular direction (i.e. horizontal direction) [27, 33].

In the past few years, many efforts have been devoted to decipher the mechanisms of anisotropy. The focus was mainly placed on the geometrical features of the Si-rich network, for instance the orientation, size and connectivity. Combining micropillar compression experiments and crystal plasticity finite element simulations, Li et al. [34] revealed that the strength anisotropy is mainly induced by the elongated Si-rich network, as it exhibits a stronger load bearing capacity and thus renders a higher flow stress in the vertical direction. The same conclusion has been reached by Song et al. [35] who investigated the anisotropy in both strength and damage initiation from the perspective of phase stress partition and showed that the anisotropy was notably influenced by the strength of the Al phase. Moreover, Wang et al. [36] and Chen et al. [37] showed that samples with similar MP structures but globularized Si phase after post-heat treatment presented a steeply weakened anisotropy, confirming the key role of the Al-Si cellular structure in anisotropic strength. The anisotropy in ductility was mostly proposed to arise from the strain localization at the MPBs, promoting earlier fracture along the vertical loading direction. Chen et al. [38] studied the local strain distribution, void growth and crack nucleation in the MPB regions via in situ X-ray tomography tensile testing, and they proposed that the fracture of LPBF AlSi10Mg was mainly induced by the microvoids and cracks formed in MPBs. Fite et al. [39] also observed strain localization at MPBs in the vertical loading direction with in situ tensile tests and digital image correlation (DIC) analysis, and they showed that the local strain was correlated to the Al-Si cell size and Si network connectivity. Otani et al. [40] quantitatively characterized the strain localization within MPB in both horizontal and vertical loading directions by DIC analysis and in situ observations of deforming samples. The strain localization degree at MPBs was revealed to vary notably under different geometrical relations of the MPBs with the loading direction (LD), which was proposed to be responsible for the anisotropy in ductility. However, whether the strain localization behavior changes with microstructures induced by different LPBF parameters remains unexplored.

The aforementioned studies were mostly focused on one specific microstructure and one hierarchy, i.e. either the Al-Si cellular structure (mechanism: load bearing capacity of the Si-rich network) or the melt pool (mechanism: deformation compatibility between MPBs and MP interiors). However, the interplay and competition between the mechanisms at these two hierarchical levels are still unclear. Moreover, it will be interesting to explore whether the local deformation behaviors change with different microstructures (Al-Si cell size, melt pool border width, etc.). This paper is devoted to decipher how the microstructure heterogeneity determines the mechanical behavior of LPBF AlSi10Mg, in terms of strength, ductility and their anisotropies. To this end, two materials presenting different Al-Si cellular structures and MPB features were investigated by tensile tests with macro DIC (to obtain global strength and ductility) and in situ tensile tests with high resolution DIC (to correlate strain distribution with microstructure). Moreover, crystal plasticity finite element modeling (CPFEM) and simulations of Al-Si cellular structures of different melt pool zones were performed to assess the deformation behavior and propensity to damage of the melt pool interiors and borders. In the light of the experimental and numerical results, the main factors controlling the mechanical anisotropy were thoroughly discussed.

2. Materials and experiments

2.1 Material manufacturing

The LPBF AlSi10Mg samples were manufactured by an EOS M290 machine offering the possibility to preheat the build platform. Plates of 5×35×150 mm were printed with laser power of 390 W, layer thickness of 30 μm, hatch spacing of 0.19 mm, scanning speed of 1300 mm/s and 67° scan rotation between layers. Considering the fact that build platform preheating is recognized as an important factor determining the microstructure of LPBF AlSi10Mg [24], two different build platform temperatures, i.e. 35 ℃ and 200 ℃ were used. The preheating leads to weaker cooling speed and temperature gradient, therefore rendering a relatively coarser microstructure, as discussed in our previous work [25]. The printed samples remained in the as built state for the following characterizations.

2.2 Microstructure characterization

Scanning electron microscopy (SEM) and electron backscatter diffraction (EBSD) were employed to characterize the microstructure of the samples. Metallurgical polishing was conducted to obtain appropriate surface quality. The SEM observations were carried out with a JSM-IT500A equipment. Fig. 1(a) and (b) shows the morphologies of the three distinct zones of melt pool, i.e. FMP, CZM and HAZ for the 35 ℃ and 200 ℃ cases, respectively. Compared to the FMP, the Si-rich network is coarser in the CMP and its connectivity is notably degraded in the HAZ. The 200 ℃ material has a coarser microstructure in three aspects, first, the Al-Si cellular structure is larger in terms of cell size and wall thickness; second, the nano-particles within the Al matrix are bigger; third, the CMP and HAZ (i.e. the MPB) are wider. Nevertheless, the melt pool width and depth are very similar between the two manufactured materials.

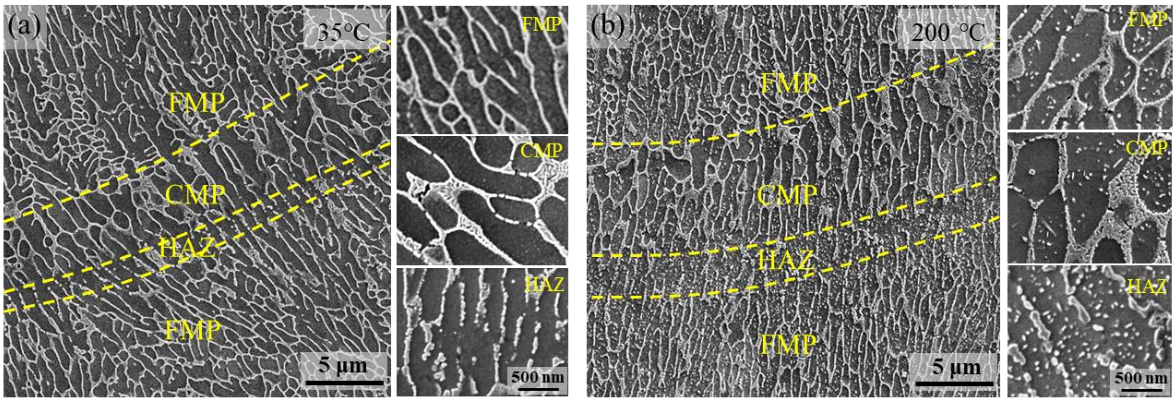

Fig. 1. Microstructure features of the 35°C (a) and 200°C (b) materials.

The EBSD characterization was performed with the EDAX S800 GMH EBSD system, using an acquisition step size of 0.5 μm. The post-processing of EBSD data was performed with the AZtecCrystal software. The inverse pole figures are presented in the supplementary material, see Fig. S1. The two materials are found to present similar grain morphologies and orientation distributions.

2.3 Mechanical tests

Uniaxial tensile tests were performed along two loading directions, one parallel (namely horizontal (H)) and the other perpendicular (namely vertical (V)) to the building direction, respectively, see Fig. 2(a). To more easily recognize the combination of build platform temperature and loading direction, the samples are further designated as 35H, 35V, 200H and 200V. The main dimensions of the sample are given in Fig. 2(a).

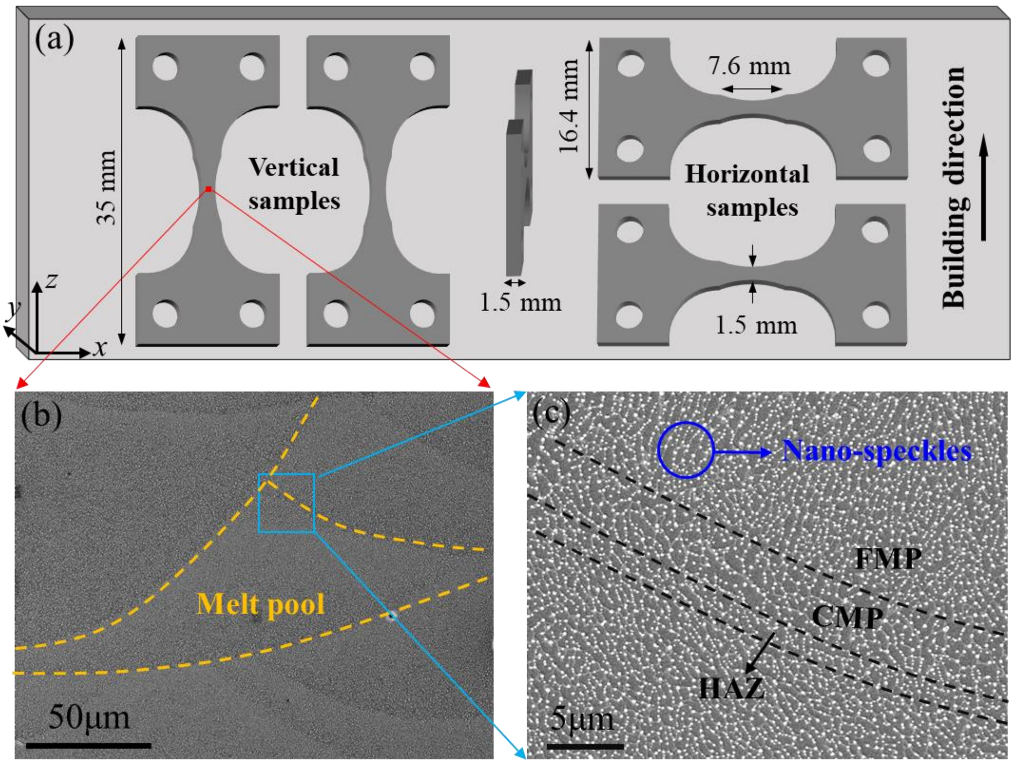

Fig. 2. Schematic drawing of vertical and horizontal samples (a), observation field of micro in situ tensile tests (b), and nanoscale speckle pattern observed at high SEM magnification (×3000) (c).

The tensile tests were performed with a Deben tensile stage, using a loading speed of 0.05 mm/min. Given the reduced gauge (with a varying cross section) length of 7.6 mm (see Fig. 2(a)), the strain rate of the tensile tests is in the order of magnitude of 10^{-4} s^{-1}. Two sets of strain measurements via digital image correlation (DIC) were carried out. The first was achieved with matte paint speckle pattern (macro-DIC) to assess the macroscopic strain field, and the second with the nanoscale gold particles (HR-DIC) to probe the strain field within the melt pools. The deposition of the nanoscale speckle pattern was conducted via an ion sputter equipment (ISC150 from Supro Instruments) at a power of 6W and spraying time of 160s, inspired by the works of Hoefnagels et al. [41] and Vermeij and Hoefnagels [42]. Such deposition is realized at room temperature so that the microstructure of LPBF AlSi10Mg will not be affected. The average size of gold speckles is roughly 150 nm, as evaluated by ImageJ. The high quality gold speckle pattern is shown in Fig. 2(b) and (c). These homogeneously distributed and dense gold particles will enable quantitative assessment of strain field in the FMP, CMP and HAZ. It is noteworthy that the Si-rich eutectic phase can be barely seen in the SEM images (taken at the magnification of 500) used for the HR-DIC analysis, see Fig. S2 in the supplementary material.

The tracking of speckle patterns during deformation was realized by an industrial camera (Baumer VCXG-25M) and a SEM (JSM-IT500A) for the macroscale and microscale strain field measurements, respectively. At least three samples were tested for macro DIC to ensure the result consistency. For the in situ SEM HR-DIC tests, a series of 5120×4096 pixel high-resolution SEM images were recorded at different deformation levels. As a note, two images were taken at each step to obtain a sufficiently large region of interest (covering 250×350 μm^2).

At least two tests were conducted for each condition. All DIC analyses were performed with the open-source code Ncorr [43].

3. Modeling and simulations

3.1 Crystal plasticity constitutive model

To probe the strength differences between the threes zones of melt pool, traditional crystal plasticity model [44-46] was used to assess the mechanical behavior of Al-Si cellular structure. In this crystal plasticity framework, the total deformation gradient is written in the form of standard multiplicative decomposition:

$$\mathbf{F} = \mathbf{F}^{*}\mathbf{F}^{p} \tag{1}$$

where $\mathbf{F}^{*}$ and $\mathbf{F}^{p}$ account for the elastic deformation and the plastic slip, respectively. The plastic velocity gradient $\mathbf{L}^{p}$ can be expressed as:

$$\mathbf{L}^{p} = \dot{\mathbf{F}}^{p}\mathbf{F}^{p-1} = \sum_{\alpha}\dot{\gamma}^{(\alpha)}\boldsymbol{s}_0^{(\alpha)} \otimes \boldsymbol{m}_0^{(\alpha)} \tag{2}$$

where $\dot{\gamma}^{(\alpha)}$ denotes the slip rate, $\boldsymbol{s}_0^{(\alpha)}$ and $\boldsymbol{m}_0^{(\alpha)}$ the slip direction vector and slip plane normal vector of the slip system α, respectively. The operator $\otimes$ refers to the Kronecker product. The slip rate $\dot{\gamma}^{(\alpha)}$ is related to the resolved shear stress on the slip system:

$$\dot{\gamma}^{(\alpha)} = \dot{\gamma}_0 \left|\frac{\tau^{(\alpha)}}{g^{(\alpha)}}\right|^{n} \mathrm{sign}(\tau^{(\alpha)}) \tag{3}$$

where $\dot{\gamma}_0$ denotes the reference strain rate, $g^{(\alpha)}$ the slip strength, n the strain rate sensitivity exponent and $\tau^{(\alpha)}$ the resolved shear stress.

The strain hardening rate $\dot{g}^{(\alpha)}$ evolves with the slip rate:

$$\dot{g}^{(\alpha)} = \sum_{\beta} h_{\alpha\beta}\dot{\gamma}^{(\beta)} \tag{4}$$

where $h_{\alpha\beta}$ denotes the slip hardening moduli, which can be classified as self-hardening $h_{\alpha\alpha}$ $(\alpha=\beta)$ and latent hardening $h_{\alpha\beta}$ $(\alpha\neq\beta)$ moduli, respectively:

$$h_{\alpha\beta}=\begin{cases} h(\gamma)=h_0\sec h^2\left|\dfrac{h_0\gamma}{\tau_s-\tau_0}\right| & (\alpha=\beta) \\ qh(\gamma) \quad (\alpha\neq\beta) \end{cases} \tag{5}$$

where h_0 denotes the initial hardening modulus, τ_0 the initial yield shear strength, τ_s the break-through stress corresponding to the initiation of large plastic flow, q the latent-hardening ratio constant (q=1.0 is generally adopted for isotropic hardening). The accumulated plastic shear strain γ is calculated by:

$$\gamma=\sum_{\alpha}\int_0^t\left|\dot{\gamma}^{(\alpha)}\right|dt \tag{6}$$

3.2 Geometrical models and simulations

To probe the difference in mechanical behavior of the three distinct zones in LPBF AlSi10Mg, six representative volume element (RVE) models were built, namely FMP35, CMP35, HAZ35, FMP200, CMP200 and HAZ200, as shown in Fig. 3. The RVEs have the same size, i.e. length = 4 μm, width = 2 μm and height = 4 μm, respectively. A constant element size of 50 nm was used for the model discretization. The volume fraction of the Si phase was set to be approximately 13.8% (FMP), 11.2% (CMP) and 10.2% (HAZ) for the two sets of models. The RVEs of the Al-Si cellular structure were built using the approach proposed by Romanova and Balokhonov [47]. The details of the model generation for FMP can be found in our previous work [35]. The CMP models were built in the same way by changing the Al cell size and the Si-rich network thickness. Table 1 presents the dimensions of the FMP and CMP models, which are determined in the light of experimental characterizations [25]. Although there are some deviations, the ratios of cell diameter, cell length and Si-network thickness between FMP and CMP are however basically consistent with the experimental characterization for both the 35 °C and 200 °C models (i.e. 0.6, 1 and 0.71 for the 35 °C model, and 0.67, 0.7 and 0.7 for the 200 °C model). Therefore, these dimensions allow to reflect the difference in mechanical behavior of different melt pool zones. As for the HAZ models, the connectivity of the networks was reduced through randomly transferring elements (roughly 70%-80%) from the Si-rich networks to the Al cells, in accordance with the FIB/SEM tomography observation [25].

Different model parameters were assigned to the 35 °C and 200 °C materials, as presented in supplementary Table S1. It is noteworthy that the Si network was modeled as elastic-plastic material following previous works based as experimental evidence of plasticity [34, 48]. Such treatment can predict comparable Si phase stress with respect to the in situ neutron diffraction measurement [49]. Moreover, only the Si network geometry changes for different melt pool zones, whereas the material parameters are the same.

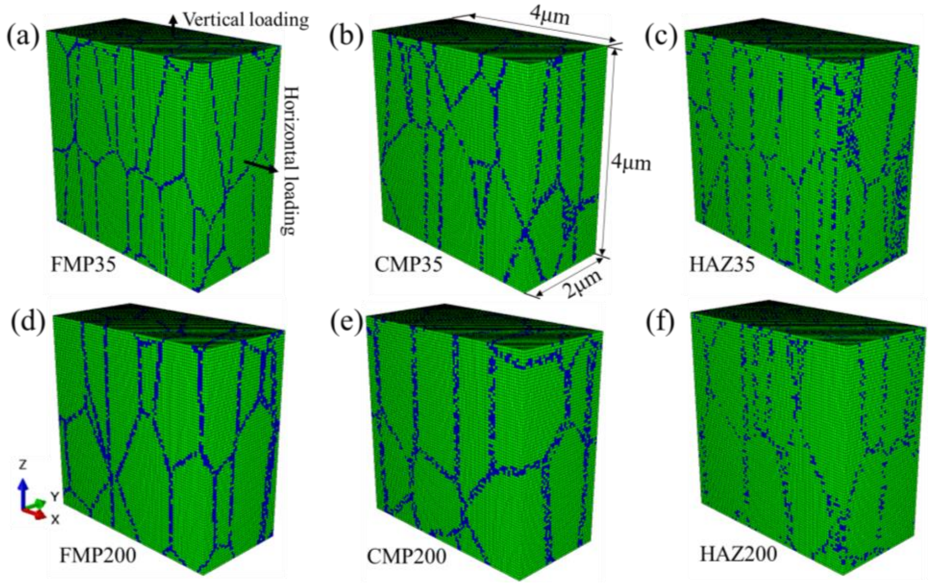

Fig. 3. Cuboid single crystal RVEs of FMP 35 (a), CMP 35 (b), HAZ 35 (c), FMP 200 (d), CMP 200

(e) and HAZ 200 (f). The vertical and horizontal loading directions are parallel and perpendicular to the building direction, respectively.

Table 1. Dimensions of the Al cell and thickness of Si-network for the FMP and CMP models.

Dimensions	FMP 35	CMP 35	FMP 200	CMP 200
Equivalent cell diameter (μm)	0.6 ± 0.15	0.83 ± 0.2	1 ± 0.3	1.21 ± 0.2
Cell length (μm)	2 ± 0.25	2 ± 0.55	2 ± 0.6	2 ± 0.75
Si-network thickness (nm)	50	100	100	150

The parameters calibrated by Li et al. [34] were adopted for the 200 °C material considering the similar macroscopic tensile properties with their printed alloy. As for the 35 °C material, the parameters for the Si network were the same as that for the 200 °C material, whereas larger τ_0, τ_s and h_0 values for the Al matrix were adopted given the higher strength induced by finer nano Si particles compared to the 200 °C material [25]. More details on the identification of the parameters can be found in our previous work [35]. All RVE models present a geometrical periodicity, and periodic boundary conditions were imposed in all three directions as:

$$u_i^{j+}(x, y, z) - u_i^{j-}(x, y, z) = c_i^j \quad (i, j = 1, 2, 3) \tag{7}$$

where u represents the displacement, i or j the three directions, j+ or j– positive or negative direction, c_1^1, c_2^2 and c_3^3 the average stretch or contraction of the RVE model due to the normal traction components, and $c_1^2 = c_2^1$, $c_1^3 = c_3^1$ and $c_2^3 = c_3^2$ the shear deformation due to the shear traction components. These constraint equations were realized by a Python script. A displacement load was then applied in either the horizontal or vertical direction to simulate the uniaxial tension. When comparing the strengths in different zones, the crystal orientation was set to [110] along the two loading directions. When comparing the strengths along different crystal orientations, [100], [110], [111] and [245] were assigned to the FMP35 and FMP200 models.

4. Results

4.1 Macroscopic tensile properties

The representative engineering stress-strain curves are shown in Fig. 4(a) and (d) for the 35 ℃ and 200 ℃ materials, respectively. Correspondingly, Fig. 4(b), (c), (e) and (f) presents the macroscale strain fields with the last images before fracture. The average tensile strength (determined from at least three samples) of the 35 ℃ material shows a similarity in the two loading directions, with the values of 482±10 MPa and 476±6 MPa for the 35V and 35H samples, respectively. The fracture strain (defined as the average local strain along the center line of the sample before fracture, see dashed lines in Fig. 4(b), (c), (e) and (f)) also changes moderately, measuring 0.099 ± 0.005 and 0.084 ± 0.01 for the 35H and 35V samples, respectively. In contrast, the 200 ℃ material exhibits a pronounced difference of tensile strength in the two loading directions, the values being 356±7 MPa and 320±5 MPa for the 200V and 200H samples, respectively. Moreover, the fracture strain is found to be higher in the horizontal direction (0.096±0.003 vs. 0.074±0.004). The anisotropy in tensile strength and fracture strain can be evaluated by $\frac{\left|\sigma_{\mathrm{UTS}}^{\mathrm{V}}-\sigma_{\mathrm{UTS}}^{\mathrm{H}}\right|}{\sigma_{\mathrm{UTS}}^{\mathrm{H}}}\times 100\%$ and $\frac{\left|\varepsilon_{\mathrm{ave}}^{\mathrm{V}}-\varepsilon_{\mathrm{ave}}^{\mathrm{H}}\right|}{\varepsilon_{\mathrm{ave}}^{\mathrm{H}}}\times 100\%$. The anisotropy values in tensile strength and fracture strain are respectively 1.3% and 15.1% for the 35 ℃ material, while they are respectively 11.3% and 22.9% for the 200 ℃ counterpart.

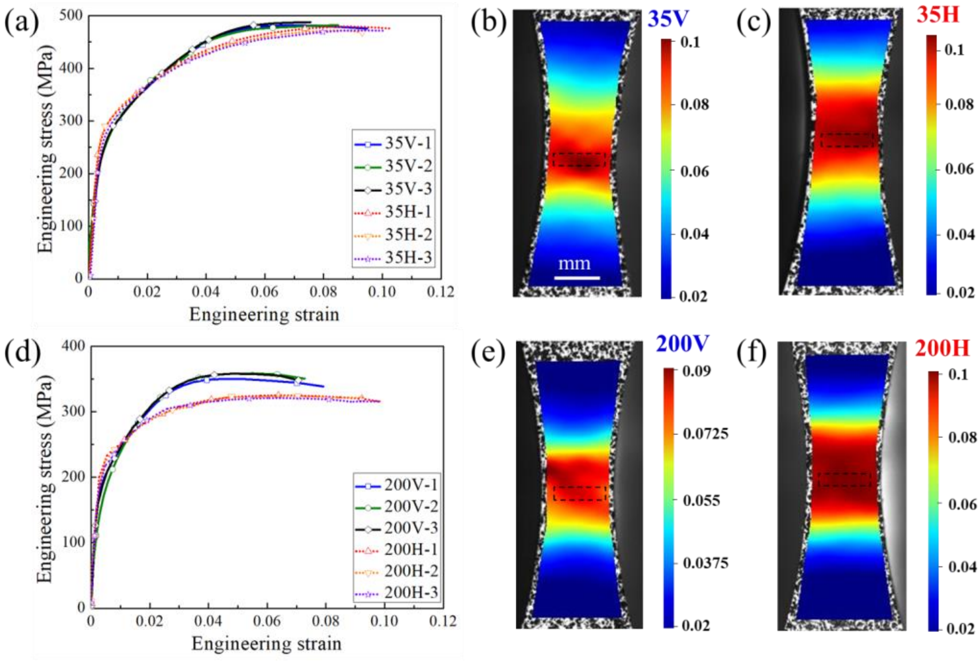

Fig. 4. Macro engineering stress-strain curves of LPBF AlSi10Mg for the 35 °C (a) and 200 °C (d) materials, DIC strain maps calculated with the last images before fracture for the 35V (b), 35H (c), 200V (e) and 200H (f) samples.

According to the above results, the 35 °C and 200 °C materials exhibit relatively weak and strong anisotropies, respectively. As mentioned in the introduction of the state of the art, the strength anisotropy has been demonstrated to result from the elongated Si-rich networks [34, 35], and the ductility anisotropy is widely believed to be induced by strain localization at the melt pool borders (MPBs) [40]. However, the interplay between the effects of the Al-Si cellular structure and the heterogeneous MPB on the strength, ductility and their anisotropies remains unclear. To further decipher the mechanisms of anisotropy and the reasons for the difference between the 35 °C and 200 °C materials, it is necessary to assess the local strain distribution with quantitative HR-DIC analysis and CPFEM simulations.

4.2 Strain distribution throughout melt pools

The results of the in situ SEM tensile tests coupled with the HR-DIC analysis are presented in Figs. 5 and 6 for the 35 °C and 200 °C materials, respectively. The subfigure (a) shows the loading curves and the location of the region of interest, (b)-(d) and (e)-(g) correspond to the strain (in the loading direction) maps at different deformation levels for the vertical and horizontal loading directions, respectively. The MPBs are highlighted by the dashed lines in the strain distribution maps, $\varepsilon_{\mathrm{ave}}$ represents the averaged strain of the whole map. It is noteworthy that the fractured specimens are presented to illustrate where the regions (field of view) of the HR-DIC analysis are located with respect to the final fracture path. Moreover, these images can also reflect the difference of fracture path between the vertical and horizontal loading directions.

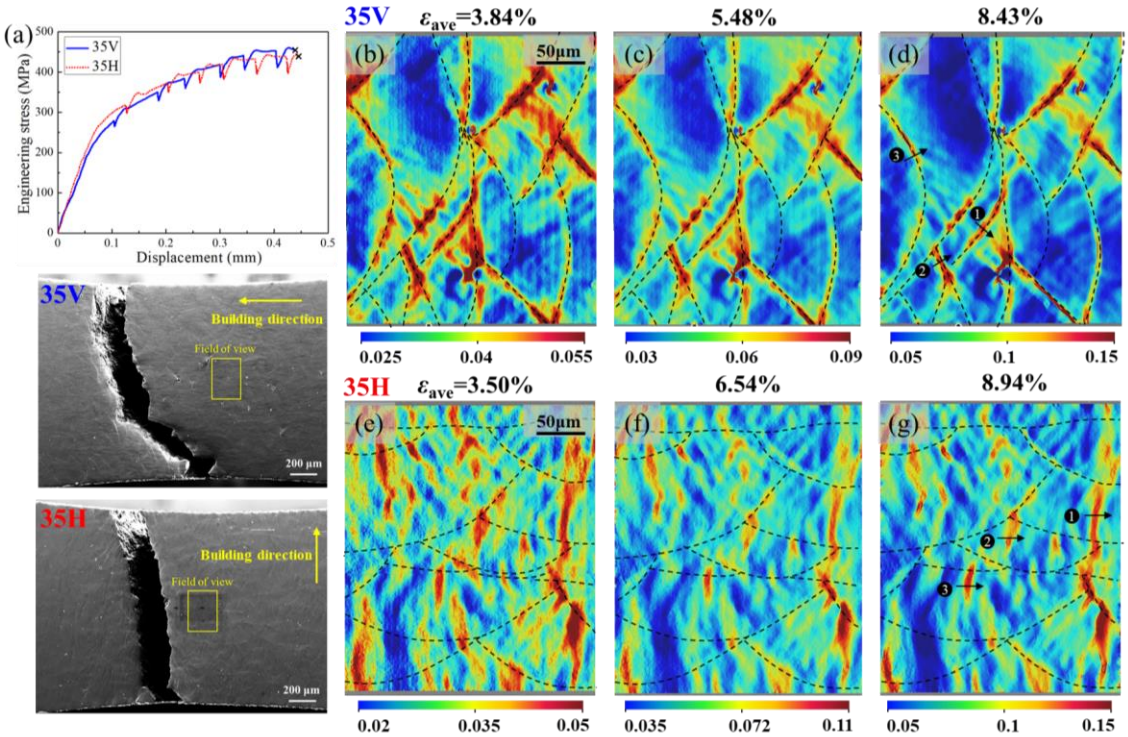

Fig. 5. In situ SEM tensile curves and observation regions for the 35 °C material (a), HR-DIC local strain distributions at different deformation levels (3.84%, 5.48% and 8.43%) for the 35V (b)-(d) and (3.50%, 6.54% and 8.94%) for the 35H (e)-(g) samples, respectively.

For the 35V and 200V samples, the deformation is highly concentrated at MPBs, where the strain values are significantly larger compared to the local strains in the melt pool interiors, as shown in Fig. 5(b)-(d) and Fig. 6(b)-(d). This behavior should be related to the lower strength of the MPBs for both the 35 °C and 200 °C materials. Interestingly, the parts of the MPBs experiencing strain localization do not show a clear geometrical relation with the loading direction, in contrast to the observations by Otani et al. [40] where the strain tends to increase when the angle between the MPB tangential and the loading direction increases.

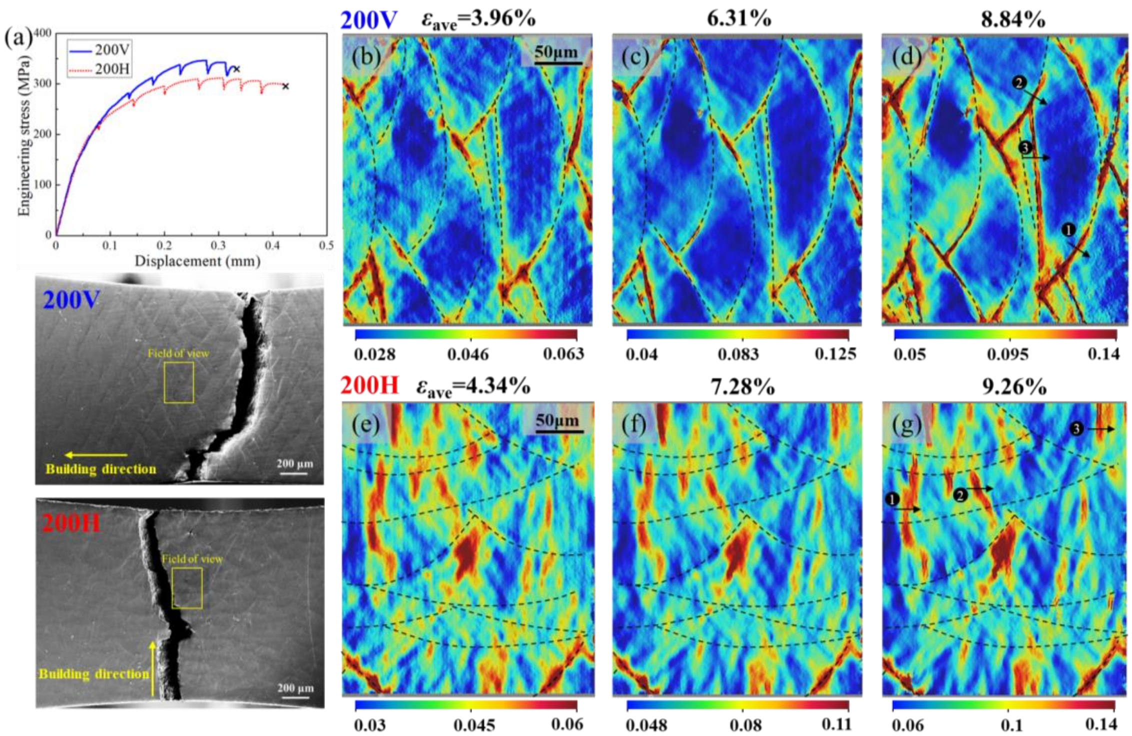

Fig. 6. In situ SEM tensile curves and observation regions for the 200 °C material (a), HR-DIC local strain distributions at different deformation levels (3.96%, 6.31% and 8.84%) for the 200V (b)-(d) and (4.34%, 7.28% and 9.26%) for the 200H (e)-(h) samples, respectively.

Regarding the 35H and 200H samples, high strain regions are also observed, as shown in Fig. 5(e)-(g) and Fig. 6(e)-(g). These regions are mostly located inside the MP interiors, exhibiting columnar shapes similar to that of the grains. On the other hand, only very few strain concentration zones are seen at the MPBs, in contrast to the vertical samples. The inhomogeneity of the strain distribution should be related to “hard” and “soft” orientations of the columnar grains, as will be assessed in the following section by CPFEM simulations.

The strain localization at the MPBs has been considered as a severe issue degrading the ductility of LPBF AlSi10Mg, especially in the vertical loading direction [29, 38, 39]. Fig. 7 reveals the distribution and evolution of the strain across the MPBs, with the strain probing lines highlighted in Figs. 5(d) and 6(d). Interestingly, the strain localization bands appear to be wider in the 35V sample (see Fig. 7(a) and (b)), albeit the 35 °C material exhibits a narrower MPB compared to the 200 °C counterpart (7 μm vs. 12 μm, see Fig. 1). This is also clearly shown in Fig. S3 in the supplementary material. For the 35V sample, the strain distribution across the MPB exhibits one wide peak (eventually two with close amplitudes), and the localization width (≈ 12 μm) is nearly twofold the MPB width (≈ 7 μm), see Fig. 7(a). For the 200V sample, the strain distribution across the MPB presents two peaks, and the distance between them is close to the HAZ width (≈ 3 μm), see Fig. 7(b). The localization width (≈ 6 μm) is nearly half the MPB width (≈ 12 μm). The evolutions of the normalized strain profile across the MPB are shown in Fig. 7(c) and (d) for the 35V and 200V samples, respectively. The strain concentration level changes slightly with the external loading for the 35V case, whereas it presents a sharp increase for the 200V case, implying a more severe strain localization at a higher global deformation.

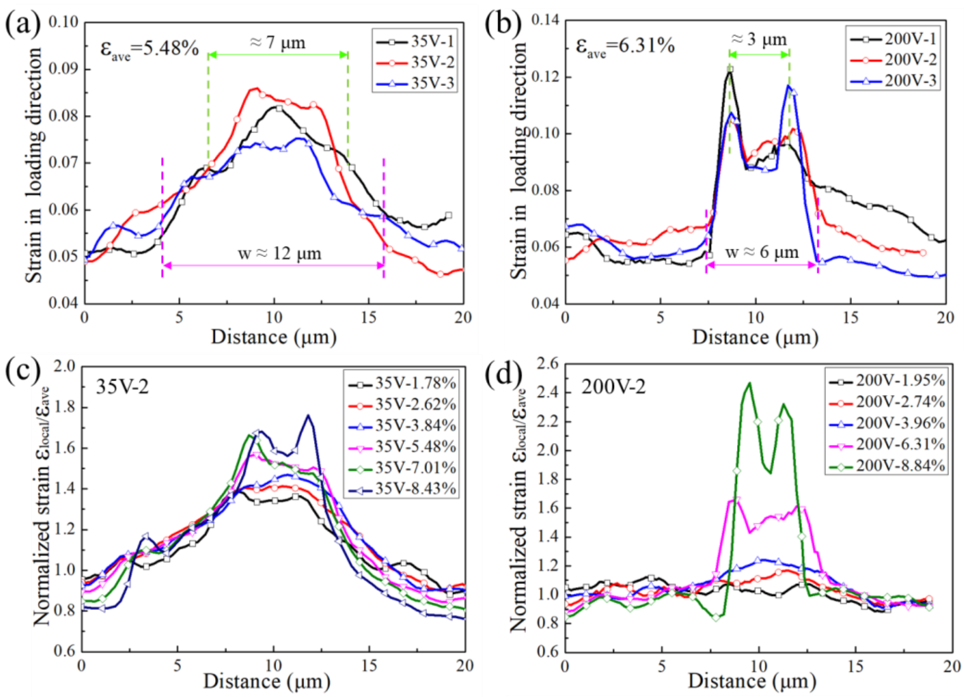

Fig. 7. Strain distributions across the MPBs for the 35V (a) and 200V (b) samples, normalized strain localization evolutions for the 35V (c) and 200V (d) samples. The distribution lines 1, 2, 3 are highlighted in Figs. 5(d) and 6(d) for the 35V and 200V samples, respectively.

Little attention has been paid to the strain localization level in the melt pool interiors along the horizontal loading direction. In order to have a clear comparison of strain localization behavior between the two loading directions, Fig. 8 displays typical strain distributions across grains exhibiting high strain levels (see the lines in Figs. 5(g) and 6(g)) and their evolutions during deformation of the 35H and 200H samples. Interestingly, the strain localization levels at the MPB in the vertical direction and across the grains in the horizontal direction are very close for the 35 °C material (Figs. 7(c) and 8(c)). In contrast, the strain localization at the MPB in the vertical sample is more severe than that across the grains in the horizontal sample (Figs. 7(d) and 8(d)) for the 200 °C material. Moreover, the strain localization behaviors are similar between the 35H and 200H samples (Fig. 8(c) and (d)).

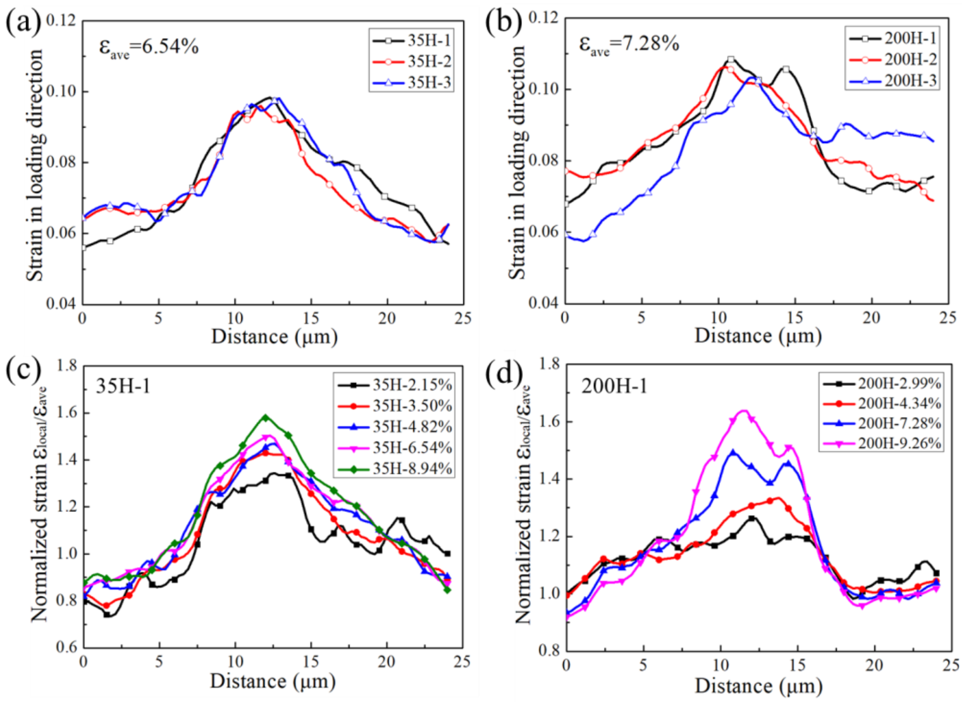

Fig. 8. Strain distributions in the MP interiors for the 35H (a) and 200H (b) samples, normalized strain localization evolutions for the 35H (c) and 200H (d) samples. The distribution lines 1, 2, 3 are highlighted in Figs. 5(g) and 6(g) for the 35H and 200H samples, respectively.

The distinct characteristics of the strain distribution between the vertical and horizontal samples imply that the microstructure experiences different strain localization mechanisms in the two loading directions. The strain localization at the MPBs should result from the lower strengths of the CMP and HAZ [27], whereas the strain localization in the MP interiors is expected to be related to the crystallographic orientations. Interestingly, the strain localization does not fully correlate to the MPB characteristics, the 35V and 200V samples present a wider and a narrower strain localization band compared to their MPB, respectively.

4.3 Microstructure related mechanical properties

The CPFEM simulations with the FMP, CMP and HAZ RVEs allow to elucidate the effect of microstructure heterogeneity on the strain localization in the 35 °C and 200 °C samples. On the one hand, the strength of the melt pool region (FMP, CMP or HAZ) is highly dependent on the size and connectivity of the Si-rich network, on the other hand, the crystallographic orientation determines the activation of slip systems, which in turn controls the strength.

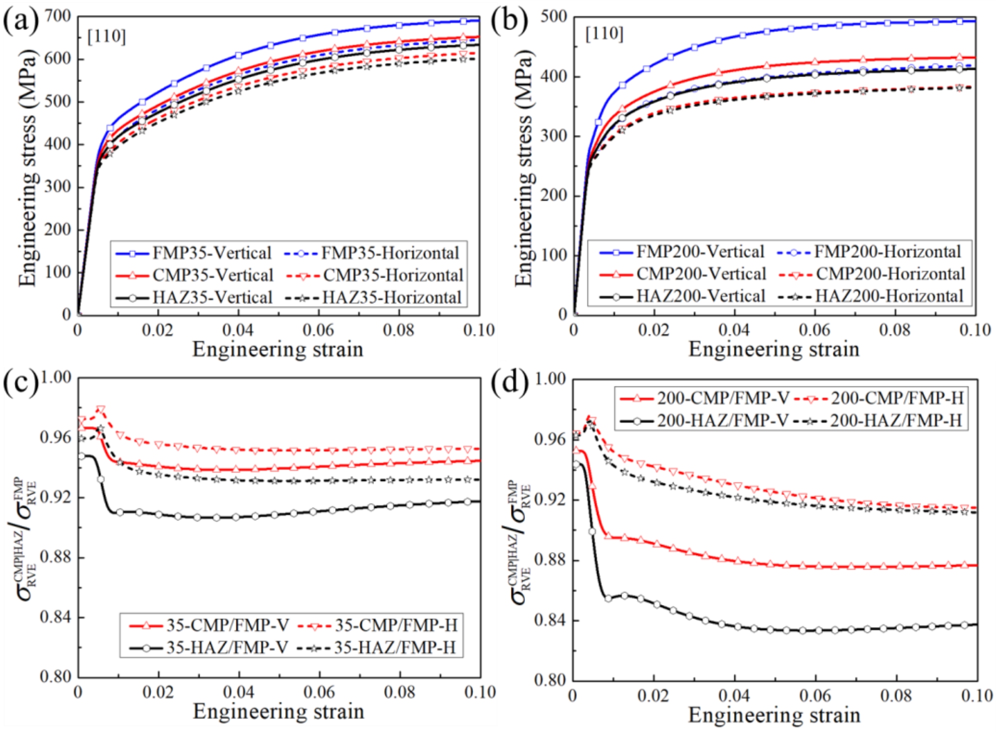

Fig. 9. Stress-strain curves of the three melt pool zones for the 35 °C (a) and 200 °C (b) models, global flow stress ratios between the two loading directions for 35 °C (c) and 200 °C (d) models. The crystal orientation is [110] for the simulation results presented in this figure.

The stress-strain curves and flow stress ratios between the FMP, CMP and HAZ (i.e. $\sigma_{\mathrm{CMP}} / \sigma_{\mathrm{FMP}}$ and $\sigma_{\mathrm{HAZ}} / \sigma_{\mathrm{FMP}}$) are shown in Fig. 9. From Fig. 9(a) and (b), it can be seen that the 35 °C Al-Si cellular structure of all three zones exhibits a weaker strength anisotropy compared with the 200 °C counterpart, confirming the notable influence of the Al matrix strength on the anisotropy [35]. Concerning the strength variation in relation to the Si-network structure, the HAZ is revealed to be the weakest zone in a given loading direction (see Fig. 9(a) and (b)), due to the highly degraded network interconnectivity. Moreover, the strength difference between the MPB and the FMP is enhanced in the vertical sample, as can be seen in Fig. 9(c) and (d). The 35 ℃ and 200 ℃ materials exhibit the same aforementioned trends, but quantitatively, the strength difference between the MPB and the MP interior is larger for the 200 ℃ material, especially for the HAZ in the vertical direction (see Fig. 9(c) and (d)). This is consistent with the narrower strain localization band (involving solely the HAZ) for the 200V sample (Fig. 7(b)).

Crystallographic orientation might also render strain inhomogeneity, especially for the horizontal loading (Figs. 5(e)-(g) and 6(e)-(g)). In this work, four typical crystallographic orientations, i.e. [110], [100], [111] and [245] were assigned to the FMP RVEs. As presented in Table S2 of the supplementary material, the [111] direction exhibits the smallest Schmid factor (0.272, with 6 active slip systems), the [245] presents a relatively high Schmid factor (0.445) but only one active slip system, the [100] and [110] crystallographic orientations have the same Schmid factor (0.408) but different numbers of active slip systems (8 vs. 4). The evolutions of the global flow stresses are presented in Fig. 10, revealing a steep influence of the crystallographic orientation on the strength. For a given loading direction, the strength along the [111] is the highest, followed by those along the [245], [110] and [100] orientations (Fig. 10(a) and (b)). From Fig. 10(c) and (d), it is found that the horizontal and vertical samples have nearly the same orientation dependence (see the solid and dashed lines for each color). Moreover, the influence of the orientation on the strength is quite similar between the 35 ℃

and 200 ℃ materials, as can be seen in Fig. 10(c) and (d). This may explain the close strain localization behaviors observed in Fig. 8(c) and (d).

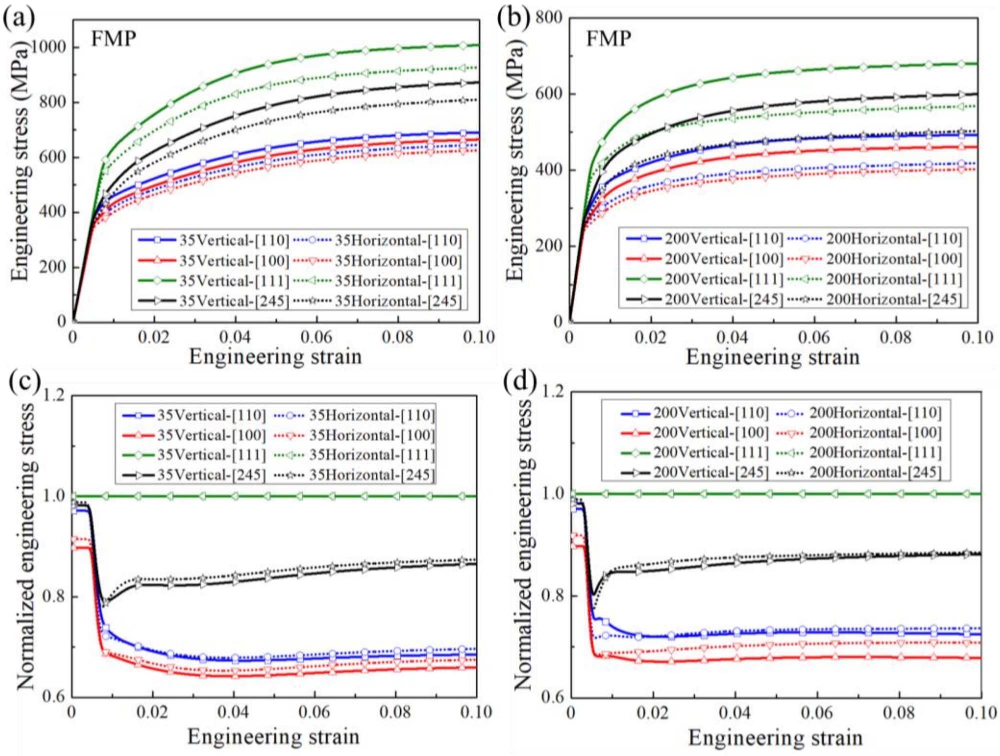

Fig. 10. Comparison of strengths between four crystallographic orientations [110], [100], [111] and [245] for the FMP 35 and FMP 200 models. Stress-strain curves for the horizontal (a) and vertical (b) loading directions, normalization over the [111] flow stress for the horizontal (c) and vertical (d) directions.

The present section has clearly revealed the influence of the microstructure heterogeneity on the mechanical strength of LPBF AlSi10Mg. On the one hand, the coarsening and connectivity degradation of the Si-rich network (i.e. the CMP and HAZ) leads to strength decrease, and such decrease is more significant for the 200 ℃ material presenting a lower strength of the Al phase, especially in the vertical direction. On the other hand, the crystallographic orientation also plays an important role in strength of the Al-Si cellular structure. Nevertheless, the FMP35 and FMP200 models show a similar sensibility to grain orientation.

5. Discussion

5.1 Anisotropy in strength

The tensile test results with macro DIC have shown a weak and a strong strength anisotropy for the 35 °C and 200 °C materials (Fig. 4), respectively. Whilst it has been demonstrated in several works that the elongated Al-Si structure (i.e. FMP) intrinsically leads to a higher strength in the vertical direction [34, 35], it remains unknown how the deformation compatibility between different melt pool zones affects the anisotropy.

In the present work, the high-resolution DIC analysis allows to quantify the strain distribution at the melt pool level and hence discern the role of the MPB in the strength anisotropy. To further reveal the deformation behavior of different zones, the strain fields are divided into the MP interiors and MPBs via separating the MPB regions from the MP interiors manually with the ImageJ software. This allows to calculate the average strains of the two regions individually. Then, the regional stress-strain curves are drawn under the assumption that the flow stress is identical throughout the melt pools, as shown in Fig. 11. This assumption might be too strong for the MPB in the vertical loading direction. Nevertheless, the regional stress of the MP interiors can well be considered equal to the global flow stress given their predominant volume compared to the MPBs ($\sigma_{\mathrm{Global}} = f_{\mathrm{MPI}}\sigma_{\mathrm{MPI}} + f_{\mathrm{MPB}}\sigma_{\mathrm{MPB}}$, with $f_{\mathrm{MPB}} \approx 0.9$). Indeed, supposing that the stress of the MPB is 20% lower than the global stress, the stress of the MP interior is only 2% higher than the global stress. Note that the assessment of MPB weakening effect mainly involves the comparison between the global curve and the MP interior regional curve (see the discussion below), the assumption can therefore be considered acceptable.

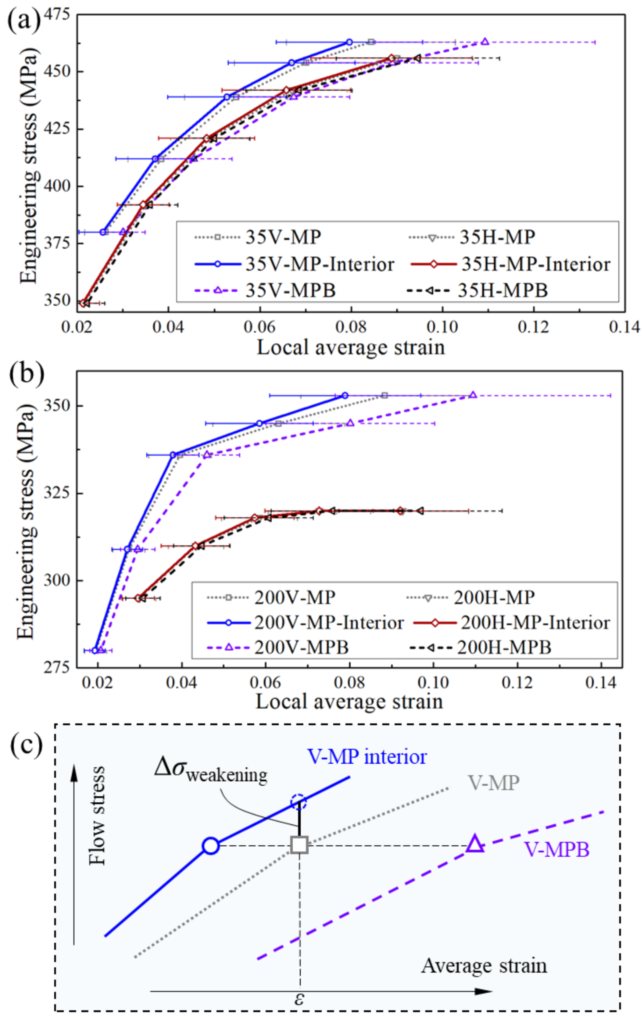

Fig. 11. Regional stress-strain curves for the 35 °C (a) and 200 °C (b) materials along the horizontal and vertical loading directions, approach for estimating the MP weakening for the vertical sample (c).

For the 35H and 200H samples, the stress-strain curves of the MP interiors and the MPBs are almost superimposed (red solid curves and black dotted curves in Fig. 11(a) and (b)), since the average strains in these two regions are nearly identical under the same stress levels. This indicates that the MPBs do not induce any weakening effects in the horizontal loading direction. In contrast, for the 35V and 200V samples, the significant strain localization at the MPBs leads to a higher average strain of the MPBs while a lower average strain of the MP interiors compared to the global strain (see Fig. 11(a) and (b)). The weakening effect of the MPB can be estimated by the approach shown in Fig. 11(c). At a certain global strain ε, the stress of the MP interiors could be identified with the blue dotted circle if there were no MPBs (assuming that the material is composed of only FMP). Nevertheless, the presence of MPBs reduces the actual strain of the MP interiors, so that the stress of the latter should be identified with the blue solid circle. Correspondingly, $\Delta\sigma_{\mathrm{weakening}}$ characterizes the weakening of the flow stress. As the stress-strain curve of the MP interiors is close to that of the whole MP region (see Fig. 11(a) and (b)), the weakened flow stress of the MP interiors due to the presence of the MPB should be very low. In this sense, the MPB does not tend to significantly affect the strength of vertical samples for both the 35 °C and 200 °C materials.

There are two reasons for the low weakening effect of the MPBs in the vertical loading direction. First, the MPBs occupy a very low volume, the strain localization would not lead the strain of the MP interiors to be far blow the global strain. Second, the strength of the MPB is not dramatically smaller than that of the MP interior, according to the CPFEM simulations (see Fig. 9). Our previous nanoindentation tests provide similar results [27]. It is noteworthy that the simulations address individually the strength of each zone, while the strain gradient developed at the MPB [20, 27] would additionally alleviate the strength difference between the MPB and the MP interior in the vertical direction.

In a nutshell, the anisotropy of LPBF AlSi10Mg, at least for the two materials presented in the present work, is still controlled by the direction dependent strength of the MP interior (i.e. FMP), which is in turn related to the elongated Si-rich network in the building direction.

5.2 Anisotropy in ductility

The 35 °C material is found to present a moderate anisotropy in ductility, whereas the anisotropy of the 200 °C counterpart is relatively stronger (Fig. 4). Nevertheless, the difference in ductility between the two loading directions is not dramatic for both materials (around 20%). In many previous investigations, the MPB has been proposed to render severe strain localization and hence lead to a much lower ductility in the vertical loading direction [32, 38, 40]. The present work has confirmed the strain localization at the MPBs of the vertical sample (Figs. 5(b)-(d), 6(b)-(d) and 7). Nevertheless, the strain localization phenomenon is also found across the columnar grains in the horizontal loading direction (Figs. 5(e)-(g), 6(e)-(g) and 8).

In fact, the strain localization cannot determine the global ductility alone, the sensibility to damage of the microstructure also plays a vital role [50]. Several previous works have demonstrated that damage initiates from the cracking of interconnected Si network in LPBF AlSi10Mg [19, 25, 51]. Considering its brittle nature, the Si phase is assumed to break (damage initiation) when its maximum principal stress (MPS) exceeds a critical value. To further reveal the damage sensibility of different MP zones under the two loading directions, the volume fraction of the Si phase presenting a MPS larger than a critical value is assessed with the CPFEM results. Herein, the critical MPS for damage initiation is set to 2.5 GPa, according to average failure stress (2 GPa) of the Si phase experimentally measured by Zhang et al. [52]. Fig. 12 shows the evolution of the volume fraction of critical Si phase as a function of the global deformation of the RVE model, bringing to light two interesting observations:

- For a given loading direction, the FMP is the most prone to damage due to the highly interconnected Si-rich network, while the HAZ presents the lowest propensity to damage due to the network collapse. The difference between the three zones is more significant for the 200 ℃ RVE models.

- For a given MP zone, loading in the vertical direction renders a higher propensity to damage, due to the elongated Si-rich networks in the building direction. Moreover, the loading direction dependence is more significant for the FMP200 and CMP200.

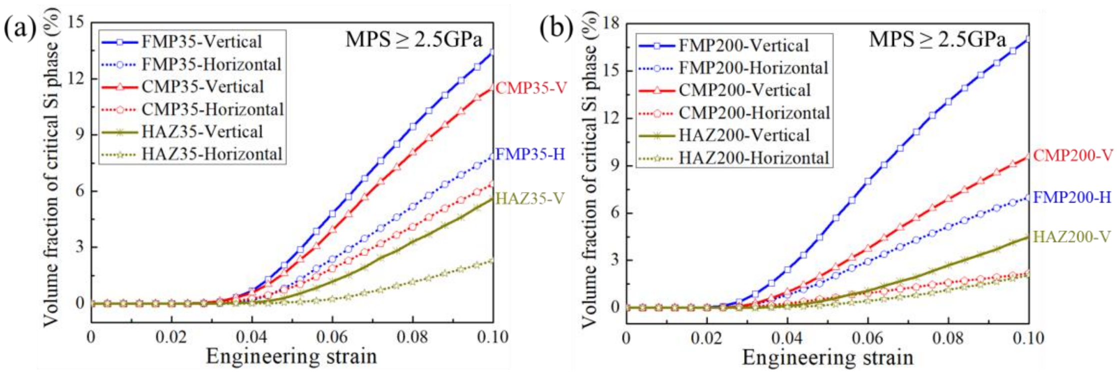

Fig. 12. Evolution of volume fraction of Si phase exhibiting a maximum principle stress (MPS) larger than 2.5 GPa for the 35 ℃ (a) and 200 ℃ (b) RVE models. The crystallographic orientation is [110].

According to our previous works [12, 27], the vertical samples generally fail along the MPBs while the horizontal ones across the MP interiors (see also Fig. S4 of the supplementary material). Combining the strain localization behavior and the sensibility to damage of the FMP-H and CMP-V/HAZ-V (see side of Fig. 12(a) and (b)), it can be inferred that the 35V sample is more prone to damage at the CMP compared to the 35H counterpart at the FMP, considering the similar strain localization level (Figs. 7(c) and 8(a)). In contrast, the HAZ-V is expected to be more sensible to damage than the FMP-H for the 200 ℃ material, given its much more significant strain localization (Figs. 7(d) and 8(b)).

Apart from the damage initiation, crack formation and propagation also influence the material ductility, as clearly shown by Hannard et al. [53]. Although the CMP-35V and HAZ-200V are more prone to damage than the FMP-35H and FMP-200H, respectively, the geometrical constraints to crack formation and propagation are however expected to be more severe along the MPBs. As illustrated in Fig. 13 (inspired from the strain localization regions in Figs. 5 and 6), the damage tends to initiate at the corners of the MPBs (i.e. strain localization zones) in the vertical samples, the connection of the damages is therefore geometrically unfavorable and the crack needs to deviate incessantly, delaying the failure. In contrast, in the horizontal samples, the geometrical constraint to damage coalescence and crack propagation is less significant. The representative crack paths for the two loading directions are also illustrated in Fig. S4 of the supplementary material. The combined effects of the propensity to damage and the constraint to damage evolution/crack propagation finally render a trivial difference in ductility between the horizontal and vertical samples.

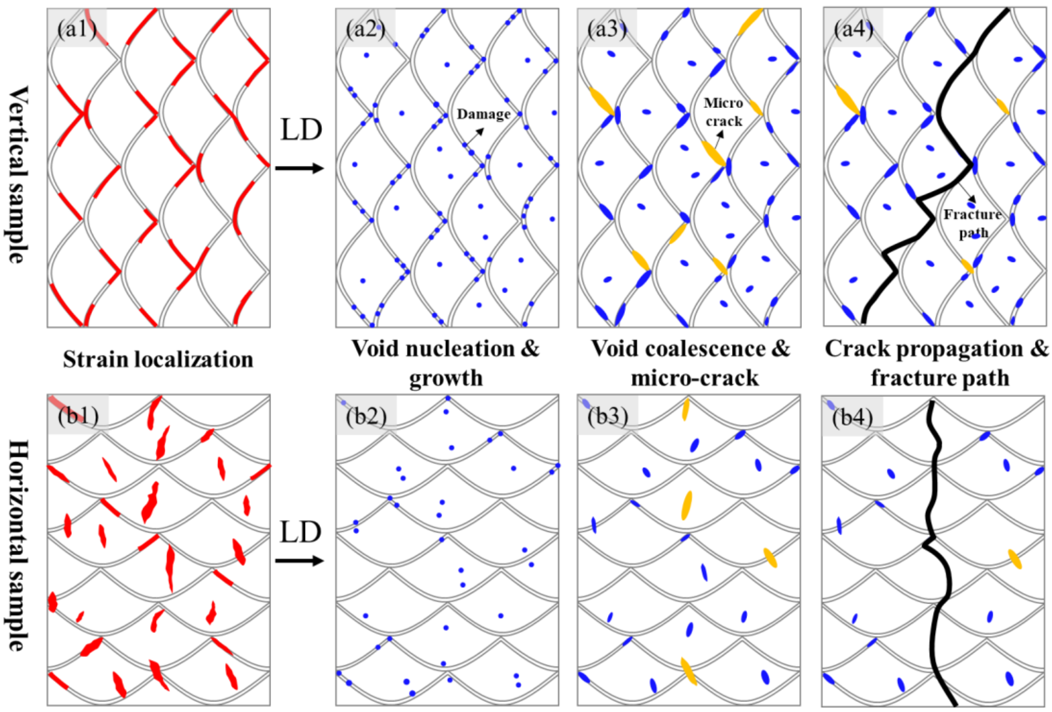

Fig. 13. Schematic drawing of damage evolution and crack propagation in the vertical (a) and horizontal

(b) samples. LD demotes the loading direction.

It is noteworthy that the 35 ℃ and 200 ℃ materials used in the present work exhibit a very low porosity (<0.05%) (see our previous work [54]), and such porosity level has been demonstrated to barely affect the ductility [55]. Therefore, the mechanical properties are mainly related to the complex microstructure. This is different from the cases with large sharp pores, where the defects are revealed to render premature failure of vertical samples and thus an important ductility anisotropy [56].

6. Conclusions

The present work investigates the mechanical behavior of two LPBF AlSi10Mg samples presenting 35 ℃ and 200 ℃ build platforms. Macro-tensile tests, in situ tensile tests/HR-DIC and crystal plasticity finite element simulations have been conducted to reveal the anisotropy in strength and ductility, the underlying mechanisms and their correlations to the hierarchical and heterogeneous microstructure. The main findings are summarized as follows:

(1) Strain localization behavior is dependent on microstructure and loading direction, it arises at melt pool border of vertical samples and across columnar grains of horizontal samples. Moreover, the localization band might be wider (35 ℃ material) or narrower than the melt pool border (200℃ material), depending on the difference in strength between the FMP, CMP and HAZ.

(2) Strength anisotropy is intrinsically induced by the elongated Al-Si cellular structure. The melt pool borders do not significantly reduce the global strength in the vertical loading direction given their low volume and strain localization effect increasing the internal flow

stress.

(3) Ductility and its anisotropy are influenced by strain localization, propensity to damage and constraints to crack formation. The vertical samples are expected to experience earlier damage initiation but delayed crack propagation along melt pool borders, therefore rendering a comparable ductility with the horizontal samples.

Acknowledgements

L.Z. and Z.L. acknowledge the supports from the NSFC (Nos. 12272143 and 12232008) and the Fundamental Research Funds for the Central Universities, China (2021XXJS116). A.S. acknowledges the WALInnov LongLifeAM project (n◦1810016) supported by the Service public de Wallonie Économie Emploi Recherche and the Starting Grant ALUFIX project (n◦716678) funded by the European Research Council (ERC).

Data availability

The data that support the findings of this study are available from the corresponding author upon reasonable request.

References

[1] D.D. Gu, W. Meiners, K. Wissenbach, R. Poprawe, Laser additive manufacturing of metallic components: materials, processes and mechanisms, International Materials Reviews 57 (2012) 133-164.
[2] S. Chowdhury, N. Yadaiah, C. Prakash, S. Ramakrishna, S. Dixit, L.R. Gupta, D. Buddhi, Laser powder bed fusion: a state-of-the-art review of the technology, materials, properties & defects, and numerical modelling, Journal of Materials Research and Technology 20 (2022) 2109-2172.
[3] Z. Wu, S. Wu, W. Qian, H. Zhang, H. Zhu, Q. Chen, Z. Zhang, F. Guo, J. Wang, P.J. Withers, Structural integrity issues of additively manufactured railway components: Progress and challenges, Engineering Failure Analysis 149 (2023) 107265.
[4] J. Fu, H. Li, X. Song, M.W. Fu, Multi-scale defects in powder-based additively manufactured metals and alloys, Journal of Materials Science & Technology 122 (2022) 165-199.
[5] N.G. March, D.R. Gunasegaram, A.B. Murphy, Evaluation of computational homogenization methods for the prediction of mechanical properties of additively manufactured metal parts, Additive Manufacturing 64 (2023) 103415.
[6] N. Sanaei, A. Fatemi, Defects in additive manufactured metals and their effect on fatigue performance: A state-of-the-art review, Progress in Materials Science 117 (2021) 100724.

[7] S. Webster, H. Lin, F.M. Carter Iii, K. Ehmann, J. Cao, Physical mechanisms in hybrid additive manufacturing: A process design framework, Journal of Materials Processing Technology 291 (2021) 117048.
[8] D. Gu, X. Shi, R. Poprawe, D.L. Bourell, R. Setchi, J. Zhu, Material-structure-performance integrated laser-metal additive manufacturing, Science 372 (2021) abg1487.
[9] Z. Zhu, Z. Hu, H.L. Seet, T. Liu, W. Liao, U. Ramamurty, S.M. Ling Nai, Recent progress on the additive manufacturing of aluminum alloys and aluminum matrix composites: Microstructure, properties, and applications, International Journal of Machine Tools and Manufacture 190 (2023) 104047.
[10] N.T. Aboulkhair, M. Simonelli, L. Parry, I. Ashcroft, C. Tuck, R. Hague, 3D printing of Aluminium alloys: Additive Manufacturing of Aluminium alloys using selective laser melting, Progress in Materials Science 106 (2019) 100578.
[11] I.M. Kusoglu, B. Gökce, S. Barcikowski, Research trends in laser powder bed fusion of Al alloys within the last decade, Additive Manufacturing 36 (2020) 101489.
[12] L. Zhao, J.G. Santos Macías, T. Douillard, Z. Li, A. Simar, Unveiling damage sites and fracture path in laser powder bed fusion AlSi10Mg: Comparison between horizontal and vertical loading directions, Materials Science and Engineering: A 807 (2021) 140845.
[13] Q. Yan, B. Song, Y.S. Shi, Comparative study of performance comparison of AlSi10Mg alloy prepared by selective laser melting and casting, Journal of Materials Science & Technology 41 (2020) 199-208.
[14] P. Van Cauwenbergh, V. Samaee, L. Thijs, J. Nejezchlebova, P. Sedlak, A. Ivekovic, D. Schryvers, B. Van Hooreweder, K. Vanmeensel, Unravelling the multi-scale structure-property relationship of laser powder bed fusion processed and heat-treated AlSi10Mg, Scientific Reports 11(1) (2021) 6423.
[15] W. Abd-Elaziem, S. Elkatatny, A.-E. Abd-Elaziem, M. Khedr, M.A. Abd El-baky, M.A. Hassan, M. Abu-Okail, M. Mohammed, A. Järvenpää, T. Allam, A. Hamada, On the current research progress of metallic materials fabricated by laser powder bed fusion process: a review, Journal of Materials Research and Technology 20 (2022) 681-707.
[16] M. Hesselmann, D. Knoop, J. Epp, V. Uhlenwinkel, A. von Hehl, A. Toenjes, Effect of precipitation-forming elements in a near-eutectic Al-Ce alloy for Laser Powder Bed Fusion, Additive Manufacturing 57 (2022) 102959.
[17] P.A. Rometsch, Y. Zhu, X. Wu, A. Huang, Review of high-strength aluminium alloys for additive manufacturing by laser powder bed fusion, Materials & Design 219 (2022) 110779.
[18] W. Lefebvre, G. Rose, P. Delroisse, E. Baustert, F. Cuvilly, A. Simar, Nanoscale periodic gradients generated by laser powder bed fusion of an AlSi10Mg alloy, Materials & Design 197 (2021) 109264.
[19] L. Zhao, J.G.S. Macias, L.P. Ding, H. Idrissi, A. Simar, Damage mechanisms in selective laser melted AlSi10Mg under as built and different post-treatment conditions, Materials Science and Engineering a-Structural Materials Properties Microstructure and Processing 764 (2019) 138210.
[20] D.D. Ben, Y.R. Ma, H.J. Yang, L.X. Meng, X.H. Shao, H.Q. Liu, S.G. Wang, Q.Q. Duan, Z.F. Zhang, Heterogeneous microstructure and voids dependence of tensile deformation in a selective laser melted AlSi10Mg alloy, Materials Science and Engineering: A 798 (2020).
[21] E. Brandl, U. Heckenberger, V. Holzinger, D. Buchbinder, Additive manufactured AlSi10Mg samples using Selective Laser Melting (SLM): Microstructure, high cycle fatigue, and fracture behavior, Materials & Design 34 (2012) 159-169.
[22] J.G. Santos Macías, C. Elangeswaran, L. Zhao, B. Van Hooreweder, J. Adrien, E. Maire, J.-Y. Buffière, W. Ludwig, P.J. Jacques, A. Simar, Ductilisation and fatigue life enhancement of selective laser melted AlSi10Mg by friction stir processing, Scripta Materialia 170 (2019) 124-128.
[23] N. Takata, H. Kodaira, K. Sekizawa, A. Suzuki, M. Kobashi, Change in microstructure of selectively laser melted AlSi10Mg alloy with heat treatments, Materials Science and Engineering: A 704 (2017) 218-228.
[24] L. Zhao, L.B. Song, J.G.S. Macias, Y.X. Zhu, M.S. Huang, A. Simar, Z.H. Li, Review on the correlation between microstructure and mechanical performance for laser powder bed fusion AlSi10Mg, Additive Manufacturing 56 (2022) 102914.

[25] J.G. Santos Macías, T. Douillard, L. Zhao, E. Maire, G. Pyka, A. Simar, Influence on microstructure, strength and ductility of build platform temperature during laser powder bed fusion of AlSi10Mg, Acta Materialia 201 (2020) 231-243.
[26] M.J. Paul, Q. Liu, J.P. Best, X. Li, J.J. Kruzic, U. Ramamurty, B. Gludovatz, Fracture resistance of AlSi10Mg fabricated by laser powder bed fusion, Acta Materialia 211 (2021) 116869.
[27] L. Song, L. Zhao, L. Ding, Y. Zhu, M. Huang, A. Simar, Z. Li, Microstructure and loading direction dependent hardening and damage behavior of laser powder bed fusion AlSi10Mg, Materials Science and Engineering: A 832 (2022) 142484.
[28] J. Wu, X.Q. Wang, W. Wang, M.M. Attallah, M.H. Loretto, Microstructure and strength of selectively laser melted AlSi10Mg, Acta Materialia 117 (2016) 311-320.
[29] Z.H. Xiong, S.L. Liu, S.F. Li, Y. Shi, Y.F. Yang, R.D.K. Misra, Role of melt pool boundary condition in determining the mechanical properties of selective laser melting AlSi10Mg alloy, Materials Science and Engineering: A 740-741 (2019) 148-156.
[30] L. Thijs, K. Kempen, J.-P. Kruth, J. Van Humbeeck, Fine-structured aluminium products with controllable texture by selective laser melting of pre-alloyed AlSi10Mg powder, Acta Materialia 61(5) (2013) 1809-1819.
[31] B. Chen, S.K. Moon, X. Yao, G. Bi, J. Shen, J. Umeda, K. Kondoh, Strength and strain hardening of a selective laser melted AlSi10Mg alloy, Scripta Materialia 141 (2017) 45-49.
[32] J. Delahaye, J.T. Tchuindjang, J. Lecomte-Beckers, O. Rigo, A.M. Habraken, A. Mertens, Influence of Si precipitates on fracture mechanisms of AlSi10Mg parts processed by selective laser melting, Acta Materialia 175 (2019) 160-170.
[33] L.C. Araujo, A.H.G. Gabriel, E.B. da Fonseca, J.A. Avila, A.L. Jardini, R. Seno, E.S.N. Lopes, Effects of build orientation and heat treatments on the tensile and fracture toughness properties of additively manufactured AlSi10Mg, International Journal of Mechanical Sciences 213 (2022) 106868.
[34] P. Li, Y. Kim, A.C. Bobel, L.G. Hector, A.K. Sachdev, S. Kumar, A.F. Bower, Microstructural origin of the anisotropic flow stress of laser powder bed fused AlSi10Mg, Acta Materialia 220 (2021) 117346.
[35] L. Song, S. Yuan, L. Zhao, Y. Zhu, S. Liang, M. Huang, A. Simar, Z. Li, Deciphering phase stress partition and its correlation to mechanical anisotropy of laser powder bed fusion AlSi10Mg, Additive Manufacturing 71 (2023) 103594.
[36] C.G. Wang, J.X. Zhu, G.W. Wang, Y. Qin, M.Y. Sun, J.L. Yang, X.F. Shen, S.K. Huang, Effect of building orientation and heat treatment on the anisotropic tensile properties of AlSi10Mg fabricated by selective laser melting, Journal of Alloys and Compounds 895 (2022) 162665.
[37] S. Chen, Q. Tan, W. Gao, G. Wu, J. Fan, Z. Feng, T. Huang, A.W. Godfrey, M. Zhang, X. Huang, Effect of heat treatment on the anisotropy in mechanical properties of selective laser melted AlSi10Mg, Materials Science and Engineering: A 858 (2022).
[38] H. Chen, S. Patel, M. Vlasea, Y. Zou, Enhanced tensile ductility of an additively manufactured AlSi10Mg alloy by reducing the density of melt pool boundaries, Scripta Materialia 221 (2022).
[39] J. Fite, S.E. Prameela, J. Slotwinski, T.P. Weihs, Melt pool boundaries in additively manufactured AlSi10Mg: Correlating inhomogeneous deformation with local microstructure via in-situ microtensile tests, Materials Science and Engineering: A 882 (2023).
[40] Y. Otani, N. Takata, A. Suzuki, M. Kobashi, M. Kato, Microstructural origin of anisotropic tensile ductility of Al-Si alloy manufactured by laser powder bed fusion, Scripta Materialia 226 (2023) 115259.
[41] J.P.M. Hoefnagels, M.P.F.H.L.v. Maris, T. Vermeij, One-step deposition of nano-to-micron-scalable, high-quality digital image correlation patterns for high-strain in-situ multi-microscopy testing, Strain 55 (2019) e12330.
[42] T. Vermeij, J.P.M. Hoefnagels, Plasticity, localization, and damage in ferritic-pearlitic steel studied by nanoscale digital image correlation, Scripta Materialia 208 (2022) 114327.
[43] J. Blaber, B. Adair, A. Antoniou, Ncorr: Open-Source 2D Digital Image Correlation Matlab Software, Experimental Mechanics 55(6) (2015) 1105-1122.

[44] R. Hill, Rice, J., Constitutive analysis of elastic-plastic crystals at arbitrary strain, Journal of the Mechanics and Physics of Solids 20 (1972) 401-413.
[45] J.R. Rice, Inelastic constitutive relations for solids: An internal-variable theory and its application to metal plasticity, Journal of the Mechanics and Physics of Solids 19(6) (1971) 433-455.
[46] Y. Huang, A user-material subroutine incroporating single crystal plasticity in the ABAQUS finite element program, Harvard Univ (1991).
[47] V. Romanova, R. Balokhonov, A method of step-by-step packing and its application in generating 3D microstructures of polycrystalline and composite materials, Engineering with Computers 37(1) (2021) 241-250.
[48] D.K. Kim, J.H. Hwang, E.Y. Kim, Y.U. Heo, W. Woo, S.H. Choi, Evaluation of the stress-strain relationship of constituent phases in AlSi10Mg alloy produced by selective laser melting using crystal plasticity FEM, Journal of Alloys and Compounds 714 (2017) 687-697.
[49] K. Zhu, L. Song, L. Zhao, Y. Zhu, S. Liang, M. Huang, Z. Li, Numerical study on the effect of crystallographic orientation on mechanical behavior and its anisotropy of laser powder bed fusion AlSi10Mg, Journal of Alloys and Compounds 976 (2024) 173284.
[50] F. Hannard, S. Castin, E. Maire, R. Mokso, T. Pardoen, A. Simar, Ductilization of aluminium alloy 6056 by friction stir processing, Acta Materialia 130 (2017) 121-136.
[51] U. Patakham, A. Palasay, P. Wila, R. Tongsri, MPB characteristics and Si morphologies on mechanical properties and fracture behavior of SLM AlSi10Mg, Materials Science and Engineering: A 821 (2021) 141602.
[52] X.X. Zhang, A. Lutz, H. Andrä, M. Lahres, W.M. Gan, E. Maawad, C. Emmelmann, Evolution of microscopic strains, stresses, and dislocation density during in-situ tensile loading of additively manufactured AlSi10Mg alloy, International Journal of Plasticity 139 (2021) 102946.
[53] F. Hannard, A. Simar, E. Maire, T. Pardoen, Quantitative assessment of the impact of second phase particle arrangement on damage and fracture anisotropy, Acta Materialia 148 (2018) 456-466.
[54] L. Zhao, J.G. Santos Macías, A. Dolimont, A. Simar, E. Rivière-Lorphèvre, Comparison of residual stresses obtained by the crack compliance method for parts produced by different metal additive manufacturing techniques and after friction stir processing, Additive Manufacturing 36 (2020) 101499.
[55] L. Zhao, J.G. Santos Macías, L. Ding, H. Idrissi, A. Simar, Damage mechanisms in selective laser melted AlSi10Mg under as built and different post-treatment conditions, Materials Science and Engineering: A 764 (2019) 138210.
[56] Y.J. Deng, Y.W. Shi, Y.X. Li, G.D. Lai, H.W. Chai, H.L. Xie, N.B. Zhang, S.N. Luo, In situ synchrotron x-ray imaging and diffraction study of additively manufactured AlSi10Mg alloy under uniaxial tension, Materials Science and Engineering: A 886 (2023) 145702.